DISCLAIMER

Fermilab

Studies of the trigger performance of the ICARUS T600 detector at Fermilab

FERMILAB-TM-2905-STUDENT

Studies of the trigger performance of the ICARUS T600 detector at Fermilab

Riccardo Triozzi[1]* under the supervision of Angela Fava, Donatella Torretta

Abstract
In recent years, experimental neutrino anomalies were reported: if confirmed, they could hint at the existence of additional *sterile* neutrino states participating in the mixing phenomenon. The future Short-Baseline Neutrino (SBN) project at Fermilab will pursue sterile neutrino searches, by exploiting three Liquid Argon (LAr) Time Projection Chamber (TPC) detectors located on-axis along the Booster Neutrino Beam (BNB). Aside from SBND and MicroBooNE, ICARUS will be the far detector and will also be interested by the NuMI beam (off-axis). The trigger system is a key component of the detector: it is based on the coincidence of prompt signals from scintillation light in the LAr-TPC (recorded by a system of PhotoMultiplier Tubes, PMTs) with the proton spill extraction of the beam. The present system exploits a majority-based logic and may be complemented by a trigger system based on *adder boards*, that add the analog signals of the PMTs in groups of 15. Triggering on the sum may help in identifying events closer to the TPC walls, in which there is plenty of light collected by few PMTs and for which the majority condition may not be satisfied. Many tests were carried out to characterize the adder boards, both on the hardware and software sides.

Keywords
ICARUS – SBN – Neutrino – Trigger – Adders

[1] *Department of Physics and Astronomy, University of Padua, Padua, Italy*
*__Author__: riccardo.triozzi@gmail.com

Contents

1. Introduction

The ICARUS T600 detector is the biggest LAr-TPC ever realized, with the cryostats containing 760 tons of LAr. It is the far detector within the Short Baseline Neutrino program, at 600 m from the target along the Booster Neutrino Beam axis. This chapter introduces the SBN program as well as the key features of its detectors, with an emphasis on ICARUS.

1.1 The Short Baseline Neutrino program

The Short Baseline Neutrino program [1] includes three LAr-TPC detectors, located on-axis in the BNB. The Short Baseline Neutrino Near Detector (SBN-ND, or SBND), currently being built, will be located at 110 m from the BNB target. The MicroBooNE detector is located in the Liquid Argon Test Facility (LArTF) at 470 m and has presently completed its data taking, producing the world's first high statistics results on ν-Ar interactions [2]. As previously mentioned, ICARUS is located at 600 m from the BNB target, has completed its installation and commissioning in May 2022 and has started collecting beam data with both BNB and NuMI beams. The locations were chosen to maximize the sensitivity to neutrino oscillations on short baseline (hence minimizing the systematic uncertainties on the ν flux), driven by the anomalies found by the LSND and MiniBooNE experiments. The layout of the SBN project is depicted in Figure 1. The basic features of the detectors are summarized in Table 1.

In particular, the Booster Neutrino Beam is generated by extracting protons (at 8 GeV kinetic energy) from the Booster accelerator, impacting them on a Be target to produce hadrons (mostly π). A *focusing horn* focuses the charged secondaries and mesons can propagate down a 50 m-long tunnel: from

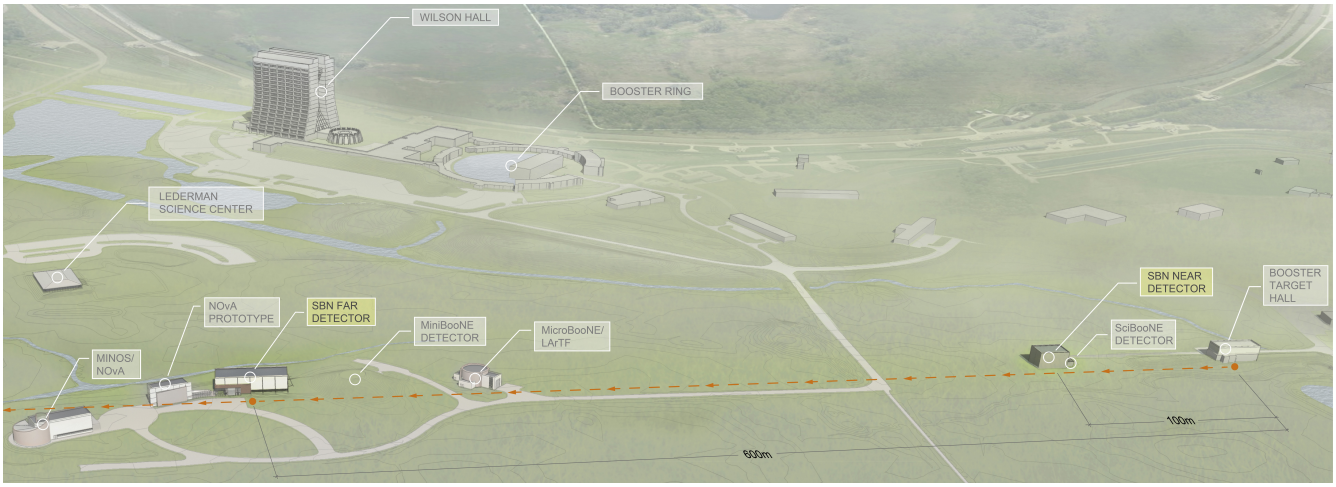

Figure 1. Short Baseline Neutrino project layout. The program includes three LAr-TPC detectors, located on axis along the Booster Neutrino Beam. From the right: SBND, at 110 m from the BNB target; MicroBooNE, at 470 m; ICARUS, at 600 m. ICARUS will be interested by the NuMI beam (off-axis) aswell.

	Baseline	Total / Active Mass
SBN-ND	110 m	220 t / 112 t
MicroBooNE	470 m	170 t / 89 t
ICARUS	600 m	760 t / 476 t

Table 1. Summary of the SBN detectors locations with respect to the Booster Neutrino Beam target, Liquid Argon total mass and active mass.

their decays, ν_μ and ν_e are produced. The remaining particles are stopped by a concrete and steel absorber.

The physics program of ICARUS is enhanced by the stand-alone studies of neutrino cross-section relevant to the Long Baseline Neutrino Facility program, thanks to the off-axis neutrinos from the NuMI beam [3]. Its flux has a higher ν_e content and overall a different energy spectrum. The NuMI beam-line has a spill duration of 8.6 μs and one neutrino event from NuMI every 150 s is expected in ICARUS. Data collected with the NuMI beam will also be exploited for searches beyond the Standard Model and dark sector analyses [4]. The two beam-lines are schematized along with the rest of the accelerator complex in Figure 2.

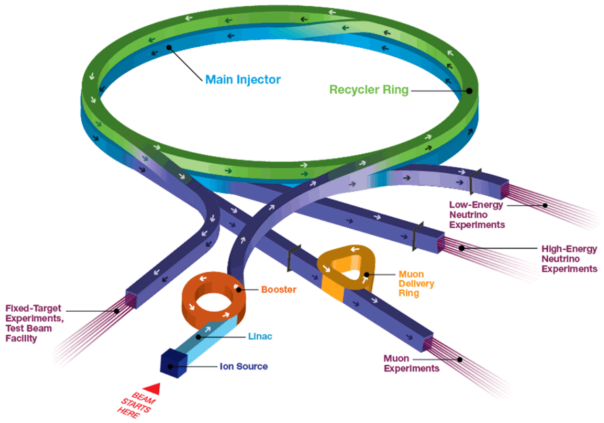

Figure 2. Schematic of the Fermilab accelerator complex. The Booster accelerator, on the left, leads to the Booster Neutrino Beam, serving low energy neutrino experiments. From the Main Injector (MI), the high energy neutrino beam NuMi is produced.

Physics Program The SBN program [1] was proposed back in 2015 to give a definitive answer to the neutrino anomalies puzzle. In the Standard Model (SM), neutrinos are neutral, left-handed and massless particles that come in three *flavours* (ν_e, ν_μ, ν_τ), linked to the corresponding leptons. They only interact via *weak interactions*, described by Charged Current (CC) and Neutral Current (NC) interactions. From studies on the Solar Neutrino Problem [5] at the beginning of the 70's, (indirect) evidence of neutrino oscillations was found: this proves that neutrinos are not massless. In fact, if neutrinos have non-zero masses, a state of fixed flavor α can be a superposition of the *mass eigenstates* (ν_1, ν_2, ν_3), hence

$$|\nu_\alpha\rangle = \sum_{i=1}^{N} U^*_{\alpha i} |\nu_i\rangle \qquad (1)$$

and a similar equation holds for antineutrinos. Note that the number of massive neutrinos N can be larger than three: in that case, the additional neutrinos must be *sterile* (i.e., they do not interact via CC or NC processes) since the number of *active* neutrinos was determined by LEP to be $N_\nu \sim 3$ [6]. Assuming that the are only 3 massive neutrinos, U is the Pontecorvo-Maki-Nakagawa-Sakata (PMNS) matrix and can be parametrized in terms of three mixing angles θ_{12}, θ_{23}, θ_{13} and one (Dirac) CP phase δ [7]. In the *oscillation* phenomenon, the flavour of a neutrino changes as it propagates through space. The probability that a neutrino oscillates from

a flavor α to a flavor β is

$$P(\nu_\alpha \to \nu_\beta) = \sin^2(2\theta)\sin^2\left(1.267\frac{\Delta m^2 L}{E_\nu}\frac{\text{GeV}}{\text{eV}^2\cdot\text{km}}\right), \quad (2)$$

in which θ is the mixing angle, $\Delta m^2 = m_2^2 - m_1^2$ is the mass square difference, L is the baseline and E_ν is the neutrino energy. Past experiments led to the determination of the mass differences $\Delta m^2_{31} \sim 2.4\cdot 10^{-3}$ eV^2 (from *atmospheric* neutrinos) and $\Delta m^2_{21} \sim 7.5\cdot 10^{-5}$ eV^2 (from *solar* neutrinos). More on the topic of neutrino oscillations can be found in [8].
In recent years, several experiments at short baselines observed anomalies [9]: if confirmed, they could hint at the presence of additional neutrino states. The anomalies can be classified in two branches:

- *reactor anomaly*: apparent disappearance signal in low energy $\overline{\nu}_e$ from nuclear reactors a few meters away from the source. This could be linked to the lack of knowledge regarding the reactor neutrino spectra and fluxes. A similar indication comes from radioactive ν_e source in Gallium solar neutrino experiments (e.g., GALLEX and SAGE). This deficit may be explained with a ν_e disappearance model, using $\Delta m^2 \geq 1$ eV^2;

- *LSND/MiniBooNE anomaly*: from the Liquid Scintillator Neutrino Detector (LSND) and MiniBooNE experiments, there is evidence for electron-like excesses in interactions with ν_μ and $\overline{\nu}_\mu$ from particle accelerators. This cannot be explained by the 3-neutrino paradigm and leads to oscillations at $L/E_\nu \sim 1\text{m/MeV}$ with $\Delta m^2 \geq 0.1$ eV^2. A strong indication in favor of such oscillations was claimed by the Neutrino-4 collaboration aswell [10].

The common interpretation of the anomalies is to theorize the presence of one (or more) additional sterile neutrino, minimally resulting in a $3+1$ neutrino mixing model. Therefore, there should be a heavy neutrino ν_4 with mass m_4, such that $\Delta m^2_{41} \sim [0.1 - 10]$ eV^2 and $m_1, m_2, m_3 \ll m_4$ [11].
The SBN physics program fits in this framework and it was set up to:

1. understand the low energy excess found in MiniBooNE, by exploiting MicroBooNE;

2. search for sterile neutrinos (e.g., testing the Neutrino-4 oscillation hypotesis) with SBN-ND and ICARUS, both in the appearance and disappearance channels;

3. further develop the LAr-TPC technology and measure the ν-Ar cross section in the GeV region for future long-baseline experiments (e.g., DUNE).

LAr-TPC Working Principle All the SBN detectors are based on the Liquid Argon Time Projection Chamber experimental technique [12], introduced by C. Rubbia in 1977 and developed by the ICARUS collaboration. The principle of operation is pictured in Figure 3.

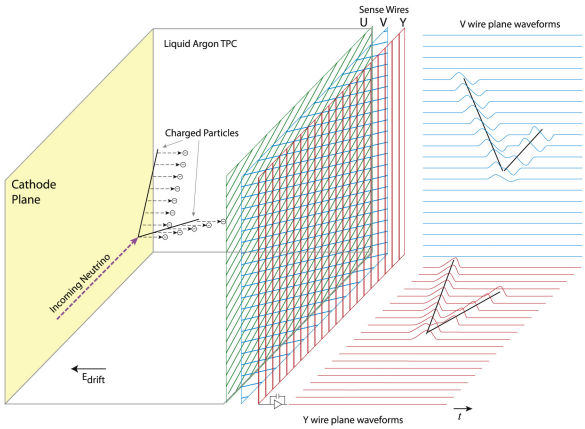

Figure 3. Working principle of the LAr-TPC technology. An incoming neutrino interacts with an Ar atom, producing charged ionizing particles. As a result, Ar^+ ions drift towards the cathode plane on the left and e^- drift towards the anode, represented by the three wire planes U, V, Y. Signals are registered for every wire.

The interaction between a neutrino and an Argon atom in the TPC produces ionizing particles: they propagate in the medium and as a result ionize and excite Argon atoms. Eventually, excited Argon atoms undergo de-excitation producing scintillation light: this constitutes a *prompt signal*, crucial for trigger purposes. Due to ionization, pair of Ar^+ and e^- form in the medium: thanks to the electrostatic field maintained in the TPC, e^- drift towards the anode and Ar^+ towards the cathode (in Figure 3, towards the left). The anode is constituted by three overlapped planes of sensing wires (with a few mm pitch). Drifting electrons produce a signal on the wires of the induction wire planes (i.e., *U* and *V*). Eventually, they produce a signal on the collection plane *Y*. Every wire is read out as a single channel and it is possible to reconstruct the ionization pattern: (*i*) in the plane perpendicular to the drift direction thanks to the angle information from the signals on (*U*, *V*, *Y*) and (*ii*) along the axis of the drift direction by combining the information on time evolution contained in the signals on (*U*, *V*, *Y*) and knowing the value of the drift velocity. The LAr-TPC technology enables for the calorimetric measurement of particle energy together with three-dimensional track reconstruction. This reproduces the imaging capabilities of *bubble chambers*, with the advantage of being electronic and scalable [1].

1.2 The ICARUS T600 Detector

The ICARUS T600 detector (Figure 4, 5) is the first large-scale LAr-TPC ever realized: the cryostats contain 760 tons of LAr, corresponding to an active mass of 476 tons of liquid Argon (kept at a temperature of 89 K) [13].

It successfully took data from 2010 to 2013 in the INFN Gran Sasso Laboratory (Italy), with cosmic rays and with the CERN Neutrinos to Gran Sasso (CNGS) beam. After an intense refurbishing activity at CERN (from 2015 until 2017),

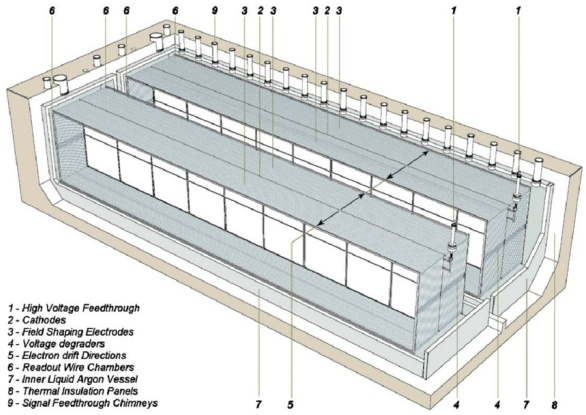

Figure 4. Schematic of ICARUS T600, composed of two identical modules (*west* and *east* cryostats). Each module houses two TPCs, separated by a common central cathode (2). The anode (6) is given by the three overlapped wire planes.

the apparatus eventually arrived at Fermilab (US), where it operates as far detector of the SBN project. The ICARUS T600 detector consists of a cryostat, split into two adjacent identical T300 modules (Figure 5), that are named *west* and *east* modules with respect to the BNB beam direction. In this section, a review of the various *detector sub-systems* operating in each module will be given.

Time Projection Chamber Each module hosts two TPCs separated by a common central cathode and a drift field of $E = 500$ V/cm is applied to the LAr volume. At the nominal field value, the 1.5 m distance between cathode and anode planes translates into a drift time of 1 ms (drift velocity $v \sim 1.6$ mm/μs). Given the low transverse diffusion in LAr, the tracks produced by ionization electron clouds are preserved and drift onto the anode. The anode of each TPC consists of three parallel wire planes 3 mm apart from each other (overall, 13312 wires per TPC). Each stainless steel wire has a diameter of 150 μm and a variable length, depending on the orientation. In fact, wires on each plane are oriented at an angle of (0°, 60° −60°) with respect to the horizontal axis. The wire coordinates on each plane are retrieved with a resolution of 1 mm^3, by combining the information of the ionizing event time with the e^- drift velocity. In this way, a three-dimensional reconstruction of the event can be obtained.

Light Collection System When a charged particle crosses the TPC, scintillation light can be produced in two ways: (*i*) excitation of Ar atoms; (*ii*) recombination of electron-ion pairs, inversely proportional to the electric field strength. The two processes lead to the production of Ar_2^* molecules, which then decay and release monochromatic VUV γ with $\lambda \sim 128$ nm. The emitted light is characterized by a *fast* ($\tau \sim 6$ ns) and a *slow* ($\tau \sim 1.5$ μs) decay components.
The scintillation light detection system is based on PhotoMultiplier Tubes (PMTs), mounted behind the wire chambers. In particular, the ICARUS T600 layout features 360 8" Hamamatsu R5912-MOD PMTs, deployed in groups of 90 devices behind each wire chamber (i.e., 90 per TPC and 180 per cryostat). A dedicated wavelength shifter (from VUV to visible) is applied to the surface of each PMT window. This system is able to guarantee a good sensitivity to ionizing events down to a 100 MeV energy deposition and also to provide the absolute timing of each interaction with $o(\text{ns})$ resolution. More on the light detection system can be found in [14].

Cosmic Ray Tagger The ICARUS T600 detector at Fermilab is situated on the surface and is exposed to a huge cosmic ray activity. As a result, the primary component of the background for various physics analyses is given by crossing cosmic rays, which could be misidentified as part of a neutrino interaction. A Cosmic Ray Tagger (CRT) system was therefore developed to fully enclose the detector and tag cosmic muons (Figure 6), removing them to identify neutrino interactions [15]. The CRT is composed of plastic scintillator modules, organized in three sub-systems (*top*, *side* and *bottom*). The scintillators are readout by Silicon PhotoMultipliers (SiPM), with the exception of the bottom system, readout by PMTs. The CRT system is fully installed and is taking data integrated with the other sub-systems since February 2022.

2. The Trigger System

The ICARUS detector has to face a ~ 0.26 Hz physical event rate within the beam gates, corresponding to ~ 23000 events per day. This comes from: (*i*) cosmic muons impinging the detector with a ~ 11 Hz rate, resulting in a signal rate of ~ 0.09 Hz for the portion of muons crossing the detector in the few μs gate windows; (*ii*) BNB, accounting for ~ 1 neutrino fully contained events every 180 spills; (*iii*) NuMI off-axis beam, with a ~ 1 neutrino event in LAr over 280 spills, plus again a contribution from cosmic rays and beam halos.
A staged level trigger system is needed to manage the huge amount of data (starting from the 5 Hz beam gate rate) and select the physical rate. A further offline step will be associating the events to the *true* neutrino interactions,

2.1 The ICARUS Trigger

The PMT-based light collection system was outlined in Section 1.2: in general, PMT waveforms are saved and exploited for timing, calorimetry and triggering. For each TPC, 90 PMTs are connected to groups of 6 CAEN V1730B digitizer boards with 16 channels each (the last channel of each board is exploited for different purposes). The boards sample the PMT signals with a rate of 500 MS/s and a 14-bit resolution. Each signal is discriminated with a threshold of 400 ADC (corresponding to 13 photoelectrons) to produce a set of Low Voltage Differential Signaling (LVDS) output signals, in terms of logic-OR of 2 by 2 adjacent PMT. The output signals of each TPC are then processed by a NI-PXIe 7820 FPGA (one per each T300 module) with a programmable logic.

Majority Trigger The majority trigger is the standard trigger system for the ICARUS detector and is based on a *majority*

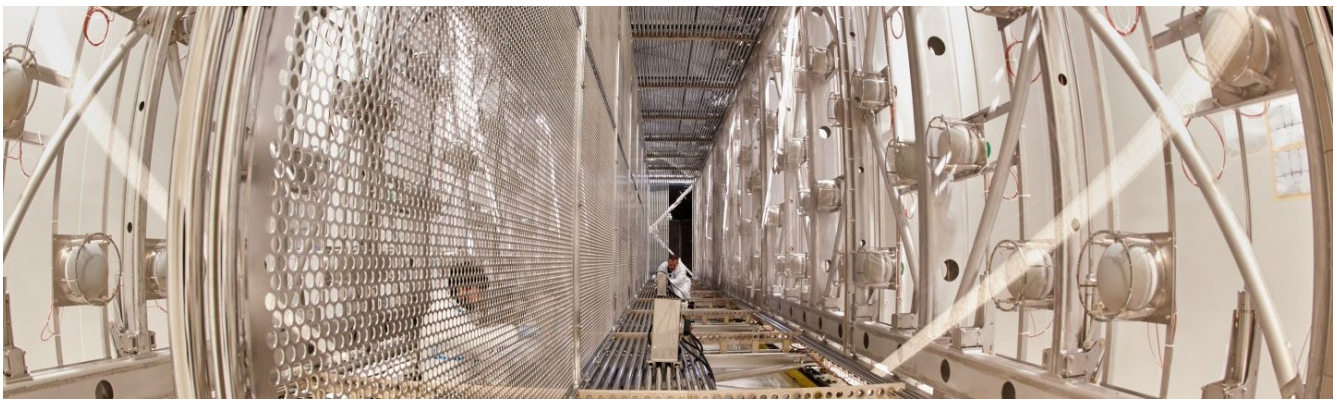

Figure 5. Picture of a ICARUS T300 module during the overhaul period at CERN. The module is composed of two TPCs, divided by the common central cathode. The PMT systems of the two TPCs are visibile at the sides, where the anode plane is located aswell. Field cages, located t the top and bottom of the TPCs, can be seen.

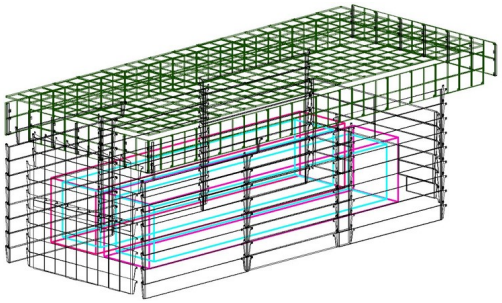

Figure 6. Schematic of the ICARUS T600 Cosmic Ray Tagger system, organized in three sections (*top*, *side* and *bottom*). Each is made from plastic scintillators of slightly different design.

logic for the generation of the PMT trigger primitive. For this purpose, each cryostat is divided in three 6 m-long windows containing 60 PMTs (30 PMTs on the west TPC and 30 on the east TPC, front-facing). In order to produce a majority trigger primitive, at least 5 LVDS signals in one the windows are needed. When the trigger primitive is temporally coincident with the beam gate (1.6 μs for BNB and 9.5 μs for NuMI time windows), a Global Trigger (GT) is produced. Note that the gate signals are synchronous with the beam spills to match regions of interesting physics activity (and are slightly longer than the actual duration of the beam spills). In the presence of a global trigger, the readout of the various detector sub-systems – TPCs (for 1.5 ms, matching the e^- drift time), PMTs, CRTs – is activated. Data are recorded in both cryostats, even if the triggering light is visible only on one T300 module.

***Local* triggers** At this point, there are different types of acquisition windows (corresponding to *local* triggers):

1. *beam trigger*: the gate signal is synchronized with the beam spill and PMT waveforms are recorded in the 28 μs around the trigger time to fully cover the spill region (this is the global trigger for ICARUS);
2. *out-of-time triggers*: shorter 10 μs-long acquisition windows for PMT waveforms are considered, given a majority-10 trigger primitive outside of the beam spill and in a 2 ms window around the global trigger. This is useful since it allows to record all the scintillation light linked to cosmic rays activity during the TPC drift time (crucial for cosmic background rejection).

MinBias Trigger In parallel, in some cases one does not want to impose any requirement on the coincidence of light, but require only the presence of a gate: this is the case for the *MinBias* trigger. In this case, there is no bias introduced by the request of PMT signals to fire a trigger. This can be done both synchronously with the beam and off-beam aswell. Note that for a single beam gate, this type of trigger cannot be used together with the majority one.
The events collected through a MinBias trigger are used for timing purposes at detector activation, for simulation studies and to have an unbiased data sample for trigger efficiency studies.

2.2 Hardware Implementation

The layout of the trigger system is based on Nation Instrument PXIe instrumentation. A single NI-1082 PXIe crate contains a NI PXIe-8840 Real Time Controller (RTC), one SPEXI board by INCAA Computers and three NI PXIe-7820R FPGAs. This is shown in Figure 7.

The SPEXI board gets the information of the neutrino beams extraction from BNB or NuMI from the White Rabbit (WR) network and generates: (*i*) the 66.6 MHz clock for the PMT digitizers; (*ii*) TT-Link trigger and clock signals for the TPC digitizers; (*iii*) a 2 ms-wide *beam enable* signal for enabling the PMT readout; (*iv*) a 1.6 μs-wide (9.5 μs-wide) beam *gate enable* signal for BNB (NuMI). As previously mentioned, two of the three FPGAs are dedicated to the PMT trigger for the two T300 modules: they evaluate the number of LVDS signal over threshold and apply the majority logic. When a Global

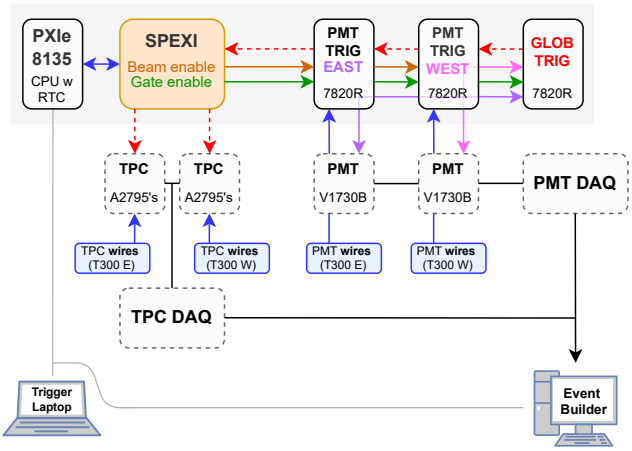

Figure 7. Representation of the trigger layout, including the PXIe Real Time Controller, the SPEXI board and the three FPGAs exploited for the trigger handling.

Trigger is present, the DAQ activates the readout of the whole detector. At the same time, the RTC retrieves the beam gate's timestamp from the SPEXI and the global trigger's timestamp and transfer the data to the DAQ via TCP/IP transfer protocol.

2.3 The Adder Trigger System

From recent global trigger efficiency studies on MC and collected data, it was found that the efficiency is at least 97% for energies greater than 300 MeV. Nevertheless, hints of lower efficiency in cosmic ray detection was found for out-of-time PMT triggers. The trigger electronics is currently based on discrimination of single PMT signals and majority patterns. This may be complemented by the exploitation of a system based on *adder* boards.

Adder Boards Each custom-made board is composed of two stages, as represented in Figure 8. The first one is the *signal splitter*: this stage is designed to recieve 15 PMT signals as inputs, leaving almost unaffected the PMT signals line towards the digitizers (95% amplitude on 50 Ω impedance) and scaling each signal by a factor 5% (again, on a 50 Ω impedance). The *adder stage* follows, in which the analog sum of the 15 scaled PMT signals is performed. The circuit for an adder board is schematized in Figure 9: notice that the 5% component is shaped with a Sallen-Key filter, characterized by a 20 ns shaping constant.
Each analog sum is then discriminated via a CAEN DT1081B Programmable Logic Unit – one for each T300 module. The module performs all the requested processing of the output lines: discrimination, TTL conversion, counting and so on. Note that the discrimination threshold has to be tuned to optimize the detection efficiency. The final output (in TTL format) will be included in the trigger logic for further signal handling via FPGA and for generating the global trigger.

Motivation The discriminated adders' output represents a source of additional trigger information. The first possible

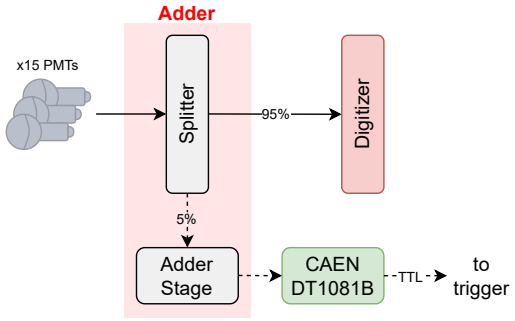

Figure 8. Representation of the adder trigger system setup. From the left: the 15 PMT signals are split into two 95% and 5% components. The first one continues to the digitizer and the adder stage sums up the 15 signals scaled by 5%. Finally, an external module is used for discrimination.

benefit comes from the fact that adders provide a complementary information on the charge, that is independent from the majority logic. In fact, if we consider events with a small detector occupancy (e.g., a cosmic track close to the corners of the detector), there may be a huge amount of light that is collected only by a small number of PMTs. By triggering on the sum, we get rid of the constraint on the number of fired PMTs. Moreover, this type of trigger system can and may be used in OR with the majority trigger to improve the efficiency below 300 MeV for CC events and generally for NC events. This can also be useful to study the relative trigger efficiency of the majority logic, allowing to monitor its performance online.

Internship Aim This research project is centred around adder board and the possible development of an adder-based trigger system. The objectives, that will be discussed in the following sections, were: (*i*) to characterize the adder board; (*ii*) to check that there is no drop in the adder trigger system performance with respect to the majority trigger configuration; (*iii*) to characterize the adders from the point of view of the waveforms; (*iv*) to define an optimal discrimination threshold and to investigate how to combine the adders with the majority trigger system.

3. Characterization of the Adders

Several tests were performed on the adder boards, in order to characterize their performance and verify their functioning. In the next section, the performance of the standard (majority) trigger system was assessed: this will serve as a benchmark for the adders' measurements.

3.1 Majority Trigger Performance

As a first test, the number of LVDS counts produced after discrimination were counted. In particular, by exploiting a dedicated LabVIEW [16] software running on the FPGAs, it was possible to get the number of LVDS signals per channel every 10 s. Each measurement had a duration of $\sim 5-10$ min-

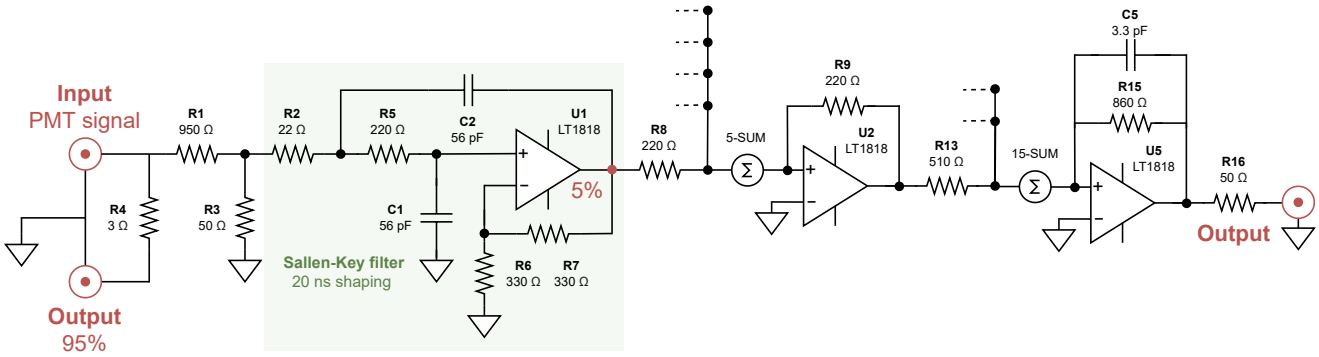

Figure 9. Scheme of an *adder board* circuit. From left to right: a *splitter* splits the signal into two 95%/5% components; the latter is shaped with a Sallen-Key filter and eventually 15 signals are summed up.

utes, resulting in sets of $\sim 30-60$ measurements per LVDS channel. This procedure was repeated for different detector configurations, by changing the drift field (i.e., the High Voltage) and the PMT discrimination threshold for LVDS signal production (an example is given in Figure 10, for a configuration with HV $= 51$ kV and a 350 ADC threshold). Since the rate is quite stable for a fixed channel, the mean over the various data blocks was considered (the error on each channel rate will be the standard error).

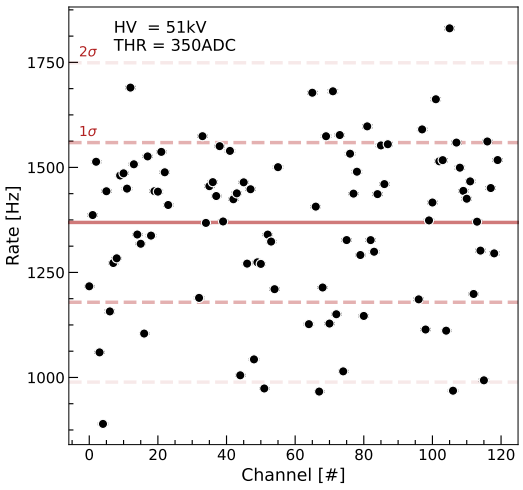

Figure 10. LVDS rate as a function of the channel number for a configuration with HV $= 51$ kV and a PMT discrimination threshold of 350 ADC. The uncertainty on the points is the data error. Mean and standard deviation are highlighted.

Drift Field Since the rate data are within three standard deviations with respect to the mean value, the mean of the rate over all the LVDS channel is considered. The first parameter that was tuned was the High Voltage (HV), tightly related to the *drift field* in TPC; the HV was set to 0 V (no field), 51 kV (intermediate configuration) and 75 kV (nominal value). The mean LVDS rate trend as a function of the LVDS discrimination threshold for the different HV values is pictured in Figure 11.

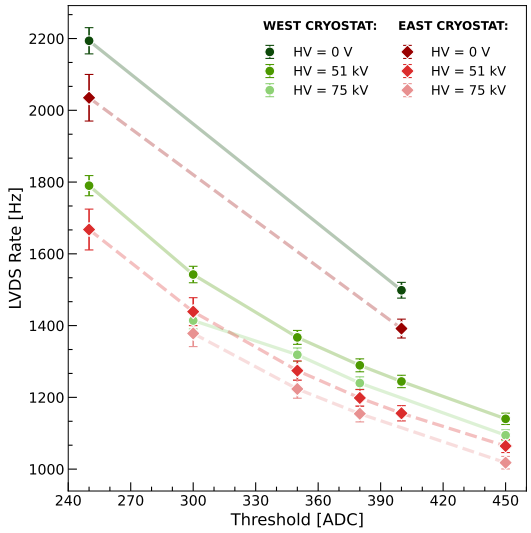

Figure 11. Mean LVDS rate as a function of the LVDS discrimination threshold for the west (in green) and east (in red) cryostats and three different drift field configurations. The rate decreases while the drift field intensity increases. There is a discrepancy of $\sim 5-10\%$ between the two cryostats.

As the drift field intensity increases, the LVDS rate decreases. Clearly, with a configuration without electric field the electrons are unable to drift towards the wire chambers (i.e., the anode): as a result, they undergo recombination and the number of flashed LVDS channels over threshold increases. Moreover, it is evident that the west cryostat has a systematically greater LVDS rate (by a factor of $\sim 5-10\%$) with respect to the east cryostat, at fixed values of LVDS threshold and HV. This phenomenon has to be thoroughly investigated.

Majorities Finally, the majority trigger logic was tested. As previously mentioned, each cryostat is divided in three *no-*

sliding windows consisting of 60 PMTs (30 on the west TPC and 30 on the east TPC) each. A dedicated LabVIEW software was implemented to count the trigger rate imposing a majority logic: in each window, a counter goes off when at least n LVDS channels are flashed (here, n ranges from 1 up to 16) within a 100 ns time window. The majority system was studied as a function of rate and threshold, with an intermediate drift field configuration of HV = 51 kV, as reported in Figure 12. It is notable that the drift field was set to an intermediate value, due to low Argon levels in the cryostats. Nevertheless, this is not an issue since the remark is on the comparison between standard majority trigger and an adder-based trigger system.

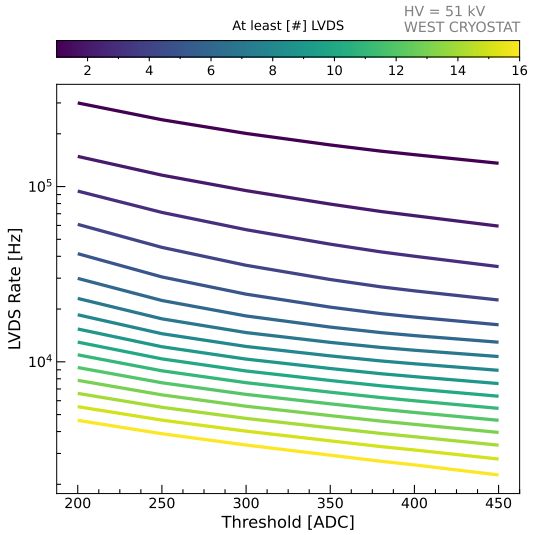

Figure 12. Mean LVDS rate as a function of the LVDS discrimination threshold for the west cryostat and HV = 51 kV, for different majority conditions. The rate decreases while the condition becomes more stringent.

In particular, the mean between the majority values in the three windows was considered for each majority logic condition. Clearly, the rate as a function of the threshold decreases while the constraint becomes more stringent.

3.2 Adders Performance

The next step was the installation of the adders: there are 24 boards in total (12 per cryostat), each with 15 input channels. Overall, the 12 boards of the west cryostat were fully cabled. Prior to any measurement, the first test that was carried out was checking the functionality of all the channels. A Tektronix AFG3252C Dual Channel Arbitrary Function Generator was used to generate a negative square pulse (1 V amplitude, 1 MHz frequency, 99% duty cycle), that was then sent to an input channel of the adder board. The input was then compared to the channel output and the board output signals on an oscilloscope. The experimental setup is schematized in Figure 13. It was observed for all channels that the signals' amplitudes do not add up to 100%: while the board output is always $\sim 5\%$ of the input as expected, the channel output is approximately the 80% (instead of the 95%). This is just a preliminary check, whose result may depend on the setup (e.g., there may be an impedance mismatch). More tests are needed, for instance using the standard DAQ of the PMT waveforms exploiting the laser calibration system.

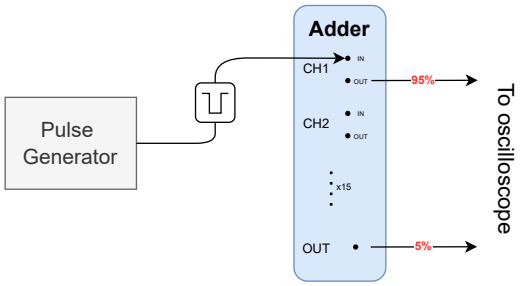

Figure 13. Representation of the experimental setup for the functionality check of the adder boards' channels.

LVDS Rate The measurement of the LVDS rates for each channel was repeated after the installation of the adders, to verify what the effect is. Recall that the digitized amplitude of the PMT signals is scaled by a factor 95%: as a result, the rate of the LVDS channels should slightly decrease with respect to the previous configuration. The result is depicted in Figure 15, for which the rate measurements were collected in the first majority window (i.e., for the first 4 adders corresponding to 60 PMTs) of the west cryostat and with a fixed drift field (HV = 51 kV). It can be seen that installing the adders resulted in a drop in LVDS rate of $\sim 3.6\%$ (mean value).

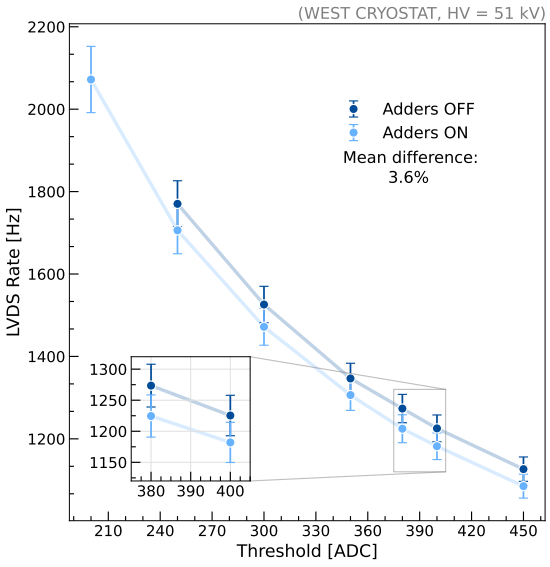

Figure 14. Mean LVDS rate as a function of the LVDS discrimination threshold for the west cryostat and a fixed drift field (HV = 51 kV), before and after having installed the adder boards.

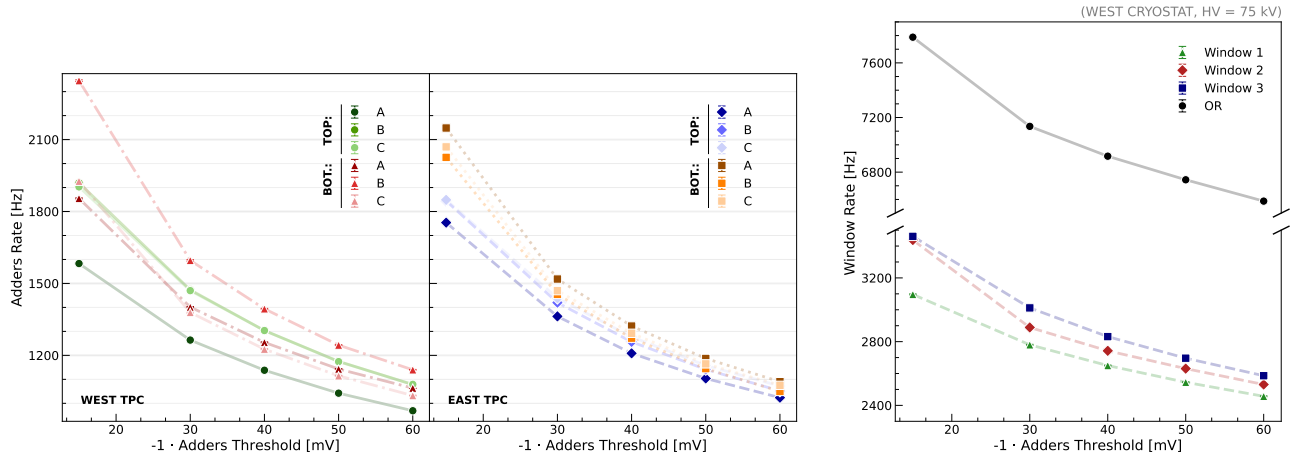

(a) (b)

Figure 15. (left) Mean adders rate as a function of the adders discrimination threshold for the west cryostat and a fixed drift field (HV = 75 kV). Adders corresponding to spacially close PMTs generally show similar rates. (right) Rate of adder-based windows as a function of the adders discrimination threshold for the west cryostat. The rate of the three windows OR is also shown for reference.

Since we would want the mean LVDS rate to be left unchanged after the adder boards are installed, the discrimination threshold for the production of LVDS signals may be lowered from 400 ADC to 380 ADC.

Adders Rate The next step is characterizing the rate of single adder boards. By using a dedicated LabVIEW software running on the trigger FPGA, the rate of single adder boards was measured as a function of the discrimination threshold for the adders, as set up on the CAEN DT1081B external module. The result for the west cryostat and a fixed drift field (HV = 75 kV) is pictured in Figure 15: note that *top* and *bottom* refer to the boards positioning within the electronics crates and are not linked to geometry. It can be observed that groups of adjacent adder boards (represented by the same color in different shades) are linked to PMTs spacially close in the TPCs and generally show similar rate values. There are some exception to this behaviour: e.g., `WW-TOP-A` (first module of the top crate, in the west TPC of the west cryostat) has an atypically lower rate. This can be explained by the fact that: (*i*) one of the PMTs is off and does not contribute to the adder signal; (*ii*) being the first adder, some of the PMTs are at the edge of the TPC, hence their coverage is reduced. On the other hand, `WW-BOT-B`'s rate is significantly increased with respect to the other modules: more tests are needed to further explore this behaviour.

Once the individual rate of each adder was characterized, the next step was to verify what is the trigger rate for a possible adder-based trigger system. The most straightforward implementation of such a trigger is to use the adder boards to define windows similar to those of the majorities. Therefore, 4 adder boards at a time were cabled in an OR logic: the adders correspond to 60 front-facing PMTs (30 in west TPC and 30 in the east TPC) corresponding to one of the three no-sliding majority windows. This logical processing of the adder output signals was implemented with the external CAEN DT1081B module and the rates were measured with a dedicated LabVIEW software. The result is represented in Figure 15 (right), where the window rate trend as a function of the adder discrimination threshold is shown for the three windows and for the global OR of the windows.

Note that if one considers the global rate value of ~ 7 kHZ at -60 mV and the fact that the time window for generating an out-of-time PMT trigger is 2 ms, this translates into approximately 14 out-of-time triggers for the west cryostat (i.e., 28 for the whole detector). One should eventually verify that this rate can be handled by the DAQ and compare these values with the majority-5 out-of-time trigger rate. If the rate is found to be unmanageable, further logic processing of the signal may be needed (e.g., creating logic coincidences between the adder outputs to lower the rates).

4. Software Analysis

Another key ingredient of the characterization of the adders is the analysis of the waveform of the adder output, with the intent of: (*i*) comparing the shape of an adder waveform to PMT signals; (*ii*) studying the characteristics of the waveforms (e.g., by building distributions of amplitude, noise's RMS and so on).

4.1 Emulation of Adders

The first task consisted in comparing the shape of PMT waveforms to an adder waveform's. Recall that 15 PMTs are connected to one adder board, whose channel outputs are then going into the digitizer. As a result, the PMT signals are

digitized at a 95% scale factor. Moreover, one should notice that the collected data correspond to through-going cosmic muons, it is expected that signals from different PMTs are asyncrhonous, due to: (*i*) different intrinsic PMT transit times; (*ii*) the fact that photons generated by the same cosmic track arrive to different PMTs at different times.

In order to emulate the signal processing of an adder board, the corresponding 15 PMT signals are scaled by a factor of $\sim 5.26\%$ (in principle the scale factor is 5%, but the PMT signals are scaled by 95%) and then they are summed up. This *emulation* can be then compared with the adder waveform, acquired by connecting the adder board to a spare channel of the digitizers. This is represented in Figure 16, in which data from majority run `#8889` and the board `WW-TOP-A` were taken into account. Note that 1 ns = 2 samples and that 1 ADC = 0.122 mV.

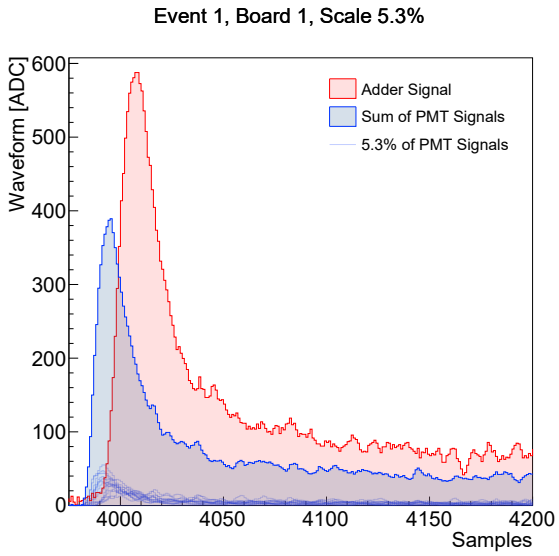

Figure 16. Comparison between digitized adder waveform (in red) and emulated waveform (in blue); the scaled PMT waveforms are also shown for reference. Data from run `#8889` and board `WW-TOP-A`.

Clearly, one can see that the emulation does not match the digitized waveform very well.

Analyzing the mismatch The first step in analyzing the mismatch was empirically tuning the scale factor in order to match the amplitudes. It was found that a scale factor of 8% leads to the waveforms having the same height. Moreover, a complete match is achieved by introducing a delay of 13 samples (i.e., 6.5 ns). The very same tuned scale factor and delay can be used for other boards and other events and lead to a good match, as highlighted by Figure 17, in which the same situation is represented for the board `WW-TOP-B` (data is from the same run as before).

Nevertheless, this tuning is explicitly empirical and does not trace back to the origin of the mismatch between emulated and digitized waveform. A possible explanation to this

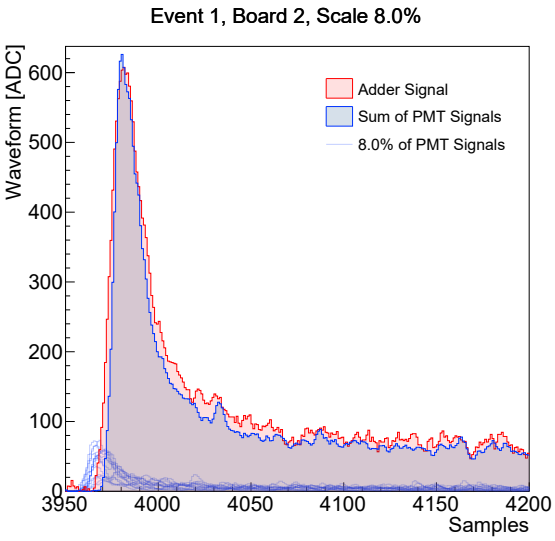

Figure 17. Comparison between digitized adder waveform (in red) and emulated waveform (in blue); the scaled PMT waveforms are also shown for reference. Data from run `#8889` and board `WW-TOP-B`. Here, the scale factor is tuned to 8% and a delay of 13 samples is introduced.

mismatch may be found in the adder circuit (Figure 9), specifically in the Sallen-Key filter in each input channel. Recall that photons from a cosmic track arrive to different PMTs spread in time (leading to asynchronous PMT pulses). As a result, the adder computes an integration of spread signals and this leads to an amplification effect that could explain the 8% scale factor. In order to verify this hypothesis, one could exploit laser pulses, since they are narrower and synchronous on all PMTs (except for the transit time) and the integration effect should be negligible.

4.2 Adder Waveform Properties

Once the signal processing of the adder board was analyzed, the next step was analyzing the properties of the adder waveforms for a given board, event-by-event. In particular, the focus was on: (*i*) signal *amplitude*, found as the height of the waveform at the peak minus the mean baseline; (*ii*) *noise RMS*, defined as the standard deviation of the baseline (i.e., non-hit samples); (*iii*) *rise time*, computed as the interval in samples between the start and the peak of the signal. The main peak in each waveform (resulting from the fast component of scintillation light) was found by means of the `TSpectrum` class within the ROOT analysis framework [17]. Note that data were cleaned up with a cut on the amplitude of the signals: by considering only events containing waveforms over 100 ADC with respect to the baseline, it was possible to cut on the electronics noise. As a result, it is possible to clearly evaluate the rise time distribution (since the quantity is defined only for signals containing a clear peak). This analysis was carried out on the digitized waveforms of the `WW-TOP-A` board and also on the first PMT, in order to compare the distributions'

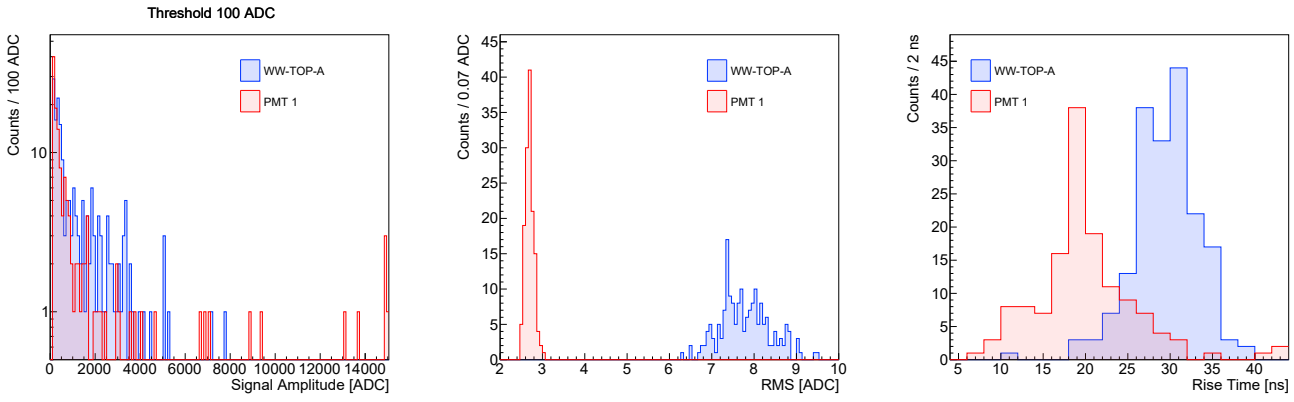

(a) (b) (c)

Figure 18. (left) Distributions of signal amplitudes: they vary over a large scale, since a majority run (`#8889`) with cosmics is considered. (center) Noise RMS distribution: adder waveforms are affected by more noise. (right) Distribution of rise times: the adder boards shape the rise time up to 30 ns.

shapes: the result is pictured in Figure 18.

Regarding the distribution of signal amplitudes, for both PMTs and adders it is possible to notice that the quantity varies over a large scale: this is expected, since data obtained with a majority run (`#8889`) are dominated by cosmic rays that, due to their geometry, have a large variability in the amount of light deposited in each cryostat. Moreover, it is evident that the adder (in red) has more signals over high threshold: this makes sense, considering the fact the an adder board gathers the waveforms of 15 PMTs.

The distribution of the noise RMS (center of Figure 18) is highlighting that the adders are overall affected by more noise than PMTs by a factor of approximately 3 ($\text{RMS}_{\text{add.}} \sim 7.8$ ADC and $\text{RMS}_{\text{PMT}} \sim 2.7$ ADC); moreover, the spread of the adders' RMS distribution is bigger by a factor of 6 ($\sigma_{\text{add.}} \sim 0.6$ ADC and $\sigma_{\text{PMT}} \sim 0.1$ ADC). In the end, this will not constitute an issue for an adder-based trigger system: the waveforms from the adder boards are big enough and the discrimination threshold will surely be higher than 100 ADC, resulting into a signal to noise ratio of at least 10.

Finally, the last plot to the right of Figure 18 shows the comparison between the rise time distributions. By considering the means of the distributions, it is clear that the PMT rise time is approximately 20 ns (shaped from an initial value of roughly 8 ns). The adder takes the rise time value to ~ 30 ns, mainly due to two factors: (*i*) *time spread*: each PMT has an intrinsic transit time of 10 ns and the adder sums up 15 non-synchronized PMT pulses; (*ii*) *geometry spread*: the positioning of PMTs varies and the trigger does not necessarily come from a PMT of the considered adder board. In the end, this won't be an issue for an adder-based trigger: one may introduce an appropriate shaping of the adder output signals before any further logic processing, in order to account for the increased rise time of the waveforms.

Adders discrimination thresholds As a final test, exploiting the digitized adders waveforms, it is possible to study the number of events over threshold as a function of the threshold. This analysis is meaningful in light of the fact that one would test whether there are any drop along the trend: that would hint at a *physically* optimal discrimination threshold. By finely varying this threshold, the number of events trend as a function of the threshold is obtained: this is depicted in Figure 19, in which the threshold was changed up to 1500 ADC (i.e., 183 mV given the 0.122mV/ADC conversion factor). This procedure was performed on `WW-TOP-A` data coming from the majority run `#8889`. Note that the error on the points is computed as the square root of the number of events, by using a Poisson distribution.

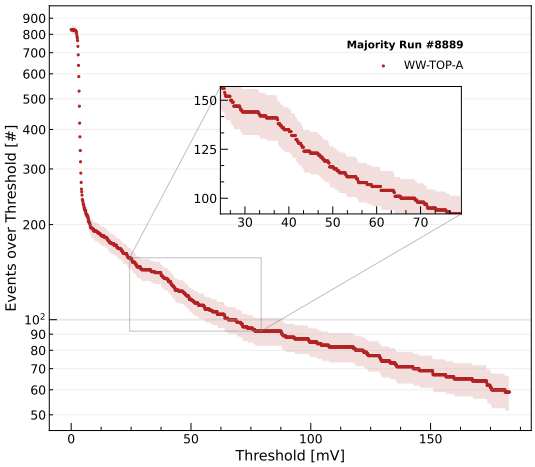

Figure 19. Number of events over threshold as a function of the threshold, expressed in mV using a conversion factor of 0.122mV/ADC. A Poisson distribution was considered for computing the uncertainty on data points. There are no drops in the trend beyond the one linked to electronics noise.

The only drop that can be observed is the one at very low values of thresholds: this is linked to a cut over the electronics noise for values above 100 ADC.

The same analysis can be performed with signals from the 15 PMTs that are connected to the considered adder board (Figure 20). In this way, the contribution of each PMT to the adder signals can be *indirectly* shown: recall that the plot does not compare the waveforms event per event, but is just showing an average trend. The trends in the tail are similar, even if there are more signals over threshold for the adder with respect to single PMTs, since it gathers 15 PMT signals.

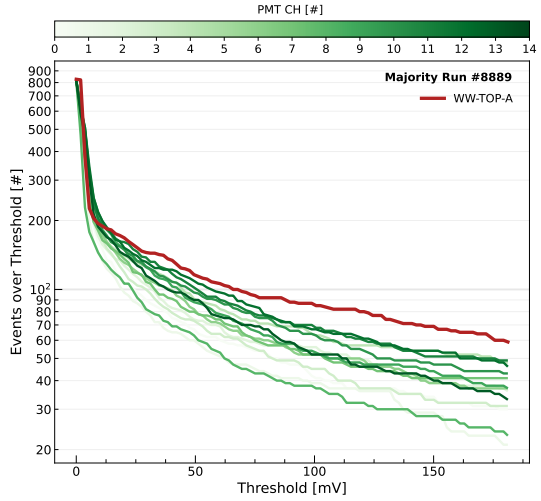

Figure 20. Number of events over threshold as a function of the threshold, expressed in mV using a conversion factor of 0.122mV/ADC. Comparison between adder and PMT trends; the error is not shown for the sake of clarity. There are no drops in the trend beyond the one linked to electronics noise.

Conclusions

The main goal of the Short Baseline Neutrino program and in particular of ICARUS is to understand past neutrino anomalies at unprecedented sensitivities with the sterile neutrino framework in mind. Being the detector installed at shallow depth, with a ~ 6 kHz expected rate of cosmic rays, the trigger system plays a central role in reducing as much as possible the rate of events to be collected and offline analysed. From early trigger efficiency studies, hints of inefficiencies in the cosmic ray detection for out-of-time local triggers based on a PMT majority condition have emerged: this may impact cosmogenic background rejection. This issue may be addressed by employing adder boards, performing an analog sum of 15 PMT signals (scaled by a factor of 5%). By triggering on the sum of signals one is able to account for events close to the PMTs, in which there is plenty of light but the majority condition of the standard trigger may be not satisfied.

In the course of this internship, the correct functionality of all the 24 adder boards was checked. After having installed the board, extensive rate measurements were carried out in order to verify that there is no drop in performance with respect to the majority trigger system. Studies showed that by setting up a simple adder-based trigger system in which the majority windows are emulated by groups of 4 adder boards in an OR logic, an adder discrimination threshold of -60 mV results in approximately 30 out-of-time local triggers. More tests are needed to verify that this rate is manageable by the DAQ. In addition, it was also possible to analyze the waveforms of the adders outputs by adding those into the data acquisition stream. As a first test, the signal processing of the adders was emulated by summing up scaled PMT waveforms: a mismatch was found, that could be originating from the shaping filter in the input channels of the adder circuit. The waveforms properties were studied and an extensive comparison between PMTs and adders was performed. By studying the event rate trend as a function of the threshold, there is no clear indication of a physics-based discrimination level for the adders and more studies are needed on this matter.

Regarding future developments of this work, it is necessary to employ laser pulses to test whether the mismatch between emulation and digitized adder waveforms come from the adder circuit shaping action or not. Moreover, one would have to investigate what the optimal threshold is based on data. In particular, there is the need to compromise between various factors like rates, trigger efficiency and the threshold itself: (i) lowering the threshold may lead to an unmanageable rate from the point of view of the DAQ; (ii) increasing the threshold leads to a decrease of the rate, but also of the efficiency (which one would want to improve with the adders). Finally, it has to be decided whether and how to implement the adders within the ICARUS trigger system, in combination with the standard trigger.

Acknowledgments

I would like to express my gratitude to the organizing committee of the Italian Summer Student Program at Fermilab, Giorgio Bellettini, Simone Donati and Emanuela Barzi, for selecting me and giving me the opportunity to work in such a thriving environment.

I am extremely grateful to my supervisors Angela Fava and Donatella Torretta for their ceaseless guidance throughout my internship work, leading to a deep understanding of my tasks.

Lastly, I gratefully acknowledge the help of the ICARUS collaboration and in particular of Gian Luca Raselli, Massimo Rossella, Andrea Scarpelli and Jacob Zettlemoyer.

References

[1] R. Acciarri et al. A proposal for a three detector short-baseline neutrino oscillation program in the fermilab booster neutrino beam, 2015.

[2] P. Abratenko et al. First measurement of inclusive muon neutrino charged current differential cross sections on

argon at $E_\nu \sim 0.8$ GeV with the MicroBooNE detector. *Physical Review Letters*, 123(13), sep 2019.

[3] Sacha E. Kopp. The NuMI neutrino beam at fermilab. In *AIP Conference Proceedings*. AIP, 2005.

[4] Brian Batell et al. Dark sector studies with neutrino beams, 2022.

[5] Masayuki Nakahata. History of solar neutrino observations, 2022.

[6] J. Beringer et al. Review of particle physics. *Phys. Rev. D*, 86:010001, Jul 2012.

[7] C. Giganti, S. Lavignac, and M. Zito. Neutrino oscillations: The rise of the PMNS paradigm. *Progress in Particle and Nuclear Physics*, 98:1–54, jan 2018.

[8] G. Bellini, L. Ludhova, G. Ranucci, and F. L. Villante. Neutrino oscillations. *Advances in High Energy Physics*, 2014:1–28, 2014.

[9] Stefan Schoppmann. Status of anomalies and sterile neutrino searches at nuclear reactors. *Universe*, 7(10):360, sep 2021.

[10] A. P. Serebrov et al. First observation of the oscillation effect in the neutrino-4 experiment on the search for the sterile neutrino. *JETP Letters*, 109(4):213–221, feb 2019.

[11] M. A. Acero et al. White paper on light sterile neutrino searches and related phenomenology, 2022.

[12] M Diwan, M Potekhin, B Viren, X Qian, and C Zhang. A novel method for event reconstruction in liquid argon time projection chamber. *Journal of Physics: Conference Series*, 762:012033, oct 2016.

[13] L. Bagby et al. Overhaul and installation of the ICARUS-t600 liquid argon TPC electronics for the FNAL short baseline neutrino program. *Journal of Instrumentation*, 16(01):P01037–P01037, jan 2021.

[14] B. Ali-Mohammadzadeh et al. Design and implementation of the new scintillation light detection system of ICARUS t600. *Journal of Instrumentation*, 15(10):T10007–T10007, oct 2020.

[15] M. Auger et al. A novel cosmic ray tagger system for liquid argon tpc neutrino detectors, 2016.

[16] LabVIEW software. Website: https://www.ni.com/en-us/shop/labview.html. Accessed: 2022-09-26.

[17] ROOT framework. Website: https://root.cern/. Accessed: 2022-10-05.